Influence of copper concentration on structural, morphological, and optical properties of tin oxide (Sn 1−x Cu x O 2−δ)

Archana verma (archanaverma8631@gmail.com)
University of Lucknow

B. Das
University of Lucknow

Research Article

Keywords: Solid-state reaction method, SnO2, (Sn1 − xCuxO2−δ)

Posted Date: September 12th, 2023

DOI: https://doi.org/10.21203/rs.3.rs-3328801/v1

Additional Declarations: No competing interests reported.

Influence of copper concentration on structural, morphological, and optical properties of tin oxide ($Sn_{1-x}Cu_xO_{2-\delta}$)

Archana verma and B.Das

(archanaverma8631@gmail.com, bdas226010@gmail.com)

Department of Physics, University of Lucknow, 226007, India

ABSTRACT

The main purpose of this article is to discuss a few advantages of Cu (transition metal) doped SnO_2 ($Sn_{1-x}Cu_xO_{2-\delta}$) bulk nanoparticles that have been prepared by applying a simple and reasonably priced technique solid-state reaction method. To analyze especially, tunning of bandgap and other structural, morphological properties of Cu-doped SnO_2 materials are examined by different innovative methods. Samples were characterized by XRD which confirms that SnO_2 has a rutile type tetragonal-shaped structure that goes to the space group $P4_2/_{mnm}$ (number 136). SEM images indicate that SnO_2 nanoparticles are inhomogeneous and densely closed with each other and an average particle size is approx 225-430 nm. The TEM images indicate that grains are present in a few cubic and spherical shapes. We observed grain size also increased (20-90nm) when we doped Copper in SnO_2 nanoparticles. UV-Vis spectroscopy inspected that the band gap of ($Sn_{1-x}Cu_xO_{2-\delta}$) sample is increased from 3.531eV to 3.701eV. XPS (X-ray Photoelectron Spectroscopy) identifies the electronic state of Sn and Cu atoms found to be 4^+ and 2^+ respectively. RAMAN spectroscopy identifies only three vibrational modes, i.e., (A_{1g}, $B_{2g,}$ and doubly degenerate E_g) in pure and Cu-doped SnO_2 nanomaterial ($Sn_{1-x}Cu_xO_{2-\delta}$)**.**

KEYWORD– Solid-state reaction method, SnO_2, ($Sn_{1-x}Cu_xO_{2-\delta}$)

1. INTRODUCTION

Metal oxides are probably the furthermost diverse, rich, and growing demand in solid-state physics, chemical science, material science, medical science, environmental studies, etc. (1). The metal oxide is used in many applications, for example, semiconductors (2), supercapacitors (3), sensors (4), piezoelectric devices (5), lithium-ion batteries (6), catalysis (7), various types of solar cells (8), energy conversion (9), rectifiers (10), electronics and optoelectronics (11). Metal oxide has magnetic, conducting, chemical, and also have electronic properties. Iron oxides, precisely ferromagnetic metal oxide (FMO), it's used in the magnetic storage device (12). The metal oxide can be used as an insulator-type material, such as sheaths for resistive heaters. Few copper oxide materials remain superconductors above liquid nitrogen temperature, so it is applicable in optical devices and the construction of mirrors (13). Metal oxide also aspect as optical properties of materials such as UV absorption, color absorption in the visible region dichroism, and photoluminescence (PL) (14). The various metals oxide (ZnO, CuO, Al_2O_3, MgO, etc) have an emergent demand in nano-medicines such as-cardiovascular diseases as a therapeutic and diagnostic cause as well as promoting wound healing. They face agglomeration and toxicity problems to show better antibacterial features against Gram-positive bacteria (15).

Scholars choose tin oxide (Stannic Oxide) as a nanomaterial because it has admirable properties such as a high energy band gap of 3.6 eV at 300 k temperature (16). Another property of tin oxide (SnO_2) is

conducting oxide with high transparency (97%) in the visible region and high reflectivity in the IR region. Further, low resistivity, and high chemical, mechanical and thermal stability are essential properties (17, 18, 19). SnO_2 NPs have been synthesized by chemical precipitation (20), thermal evaporation (21), sol-gel method (22), hydrothermal method (23), co-precipitation (24), and pyrosol process (25). Photocatalytic elements such as Zinc oxide (ZnO), titanium dioxide (TiO_2), tungsten trioxide (WO_3), ferric oxide (Fe_2O_3), copper oxide (Cu_2O), and tin dioxide (SnO_2) play a significant role in environmental applications, for example, water purification and decrease harmful ingredients in the environment (26).

Over the past few years, scholars have already reported a lot of information about transition metal (Fe, Mn, Co, Cr) doped SnO_2 nanoparticles (27,28,29) but few scholars report on the doping of copper in SnO_2 bulk nanomaterial. Therefore I incorporate copper in pristine SnO_2 because Copper oxide (transition metal) has excellent properties such as- non-toxic and native p-type semiconductors. Copper oxide has a cubic structure and it is easily available at low cost in the environment. It is used in optoelectronics, magneto electronics, microwave devices, etc (30). Another effect of Cu concentration doping on the SnO_2 for improvement of chemical sensing properties of Cu-doped SnO2 thin films (31). Therefore, in the future, I will try the effect of gas sensing on various properties of the ($Sn_{1-x}Cu_xO_{2-\delta}$) sample. in the present investigation, Cu-doped tin oxide ($Sn_{1-x}Cu_xO_{2-\delta}$) here X=0.00, 0.10, 0.20, 0.30 materials have been prepared by solid-state reaction method because it is effortless, low cost, and easy to control method. To analyze the special influence of bandgap and other structural, and morphological properties of Cu-doped SnO_2 materials are investigated and discussed systematically.

2. EXPERIMENTAL DETAIL

Firstly, the pure SnO_2 nanomaterial has been prepared by the solid-state reaction method (shown in Fig 1). In this way, we take 20 mess of metallic tin (Sigma Aldrich, 99.99%> pure) at 800 ^{0}C temperature for 4hrs in a programmable temperature-controlled Si-C furnace. After this, as prepared SnO_2 nanomaterial was grind for about 3-4hrs with the help of a mortar and pestle and found a very fine powder of pure SnO_2 nanomaterial. Doping elements (Copper oxide nanomaterial) have been prepared by the co-precipitation method. For this, high-purity chemical reagent copper chloride dehydrates ($Cucl_2.2H_2O$) procured from (Sigma Aldrich 99.99%> pure) was used as a raw material. Firstly the 1 M precursor solutions were prepared by dissolving $Cucl_2.2H_2O$ in distilled water and stirred by a magnetic stirrer for about 4hrs. After that process, an appropriate amount of ammonia solution was mixed in this solution with continuous stirring. After we left this product overnight for aging and 3-4 times washed with distilled water to remove impurities. These washed precipitates were dried in an oven at 250℃ for 4 h and ground with the help of mortar and pestle for 3-4 h to get fine particles of my sample. The obtained sample was calcined at 800^{0}C for 4 h then again ground with the help of a mortar and pestle for about several hours. The above process was repeated 2 times for better homogeneity. Finally, copper oxide was formed. In the second stage, Cu-doped tin oxide nanomaterial ($Sn_{1-x}Cu_xO_{2-\delta}$) here x=0.00, 0.10, 0.20, 030 was prepared. For this, we take the appropriate ratio of tin oxide and copper oxide were mixed them with the help of a mortar and pestle for about 3-4 hours. Finally, my sample was prepared. than few spherical pellets (~1.5 mm in thickness and ~8 mm in diameter) were being prepared with the help of a hydraulic press machine at 200 Kg /cm^2. Then these pellets of SnO_2 and ($Sn_{1-x}Cu_xO_{2-\delta}$) were kept in alumina crucibles and sintered at 900^{0}C temp in the air for 7 hrs.

To find out the influence of copper incorporation on SnO_2, pellets were characterized by X-Ray Diffractometer (XRD), UV–Vis spectroscopy, TEM (Transmission electron microscopy), Scanning Electron Microscope (SEM), RAMAN, and XPS (X-ray Photoelectron Spectroscopy). The structural identification, phase identification, and crystallite size were analyzed by XRD (Rigaku ultima IV) with monochromatic Cu-Kα radiation (λ = 0.15406 nm) at 45 Kev and 40 mA at a scan angle (2θ) of 20–80° and scanning rate of 1°/minute. The nanostructural characteristics of my sample by very high-resolution transmission electron microscopy (HRTEM-FEI Tecnai 20 G^2) were employed in both imaging and diffraction modes, using

filament LaB6 side mount and bottom mount CCDs operating at 200 Kv. Scanning Electron Microscope (Gemini SEM 300) was used to study the surface morphology of my sample. UV-Vis spectroscopy examines the absorption of a sample by ultraviolet rays. The electronic state of the element of my material is examined by X-ray Photoelectron (XPS-SPECS system) using twin anode AlKα and MgKα x-rays and RAMAN (Jobin Yvon Horibra LABRAM-HR 800 visible) examined the vibrational mode of an element of my sample.

Results and Discussion

3- Structural morphology

3.*1- XRD (X-Ray Diffraction Analysis)*

Fig 2 indicates that XRD patterns of ($Sn_{1-x}Cu_xO_{2-\delta}$) here x=0.00, 0.10, 0.20, 030, which prove that tin oxide has a tetragonal rutile structure. It is confirmed by JCPDS NO- 00-021-1250 with space group $P4_2/_{mnm}$ (number 136) (32) with no impurity nor any secondary phases detected. So The characteristic peaks are found at 2θ = 26.5, 33.8, 37.9, 38.9, 51.7, 54.7, 57.8, 61.8, 64.7, 65.9,71.2, 78.7 having (h k l) values of (110), (101), (200), (111), (211), (220), (002), (310), (112), and (301), (202), (321). The average crystalline size is calculated by Debye Scherer's formula (32) -

$$\text{Crystallite size (D)} = \frac{0.9\lambda}{\beta \cos\theta} \quad (1)$$

Where λ is the wavelength of Cu K_α radiation (1.5406A°) at a scanning rate of 1^0/min, β is the full width at half maximum (FWHM) corresponding to the diffraction angle 2θ (θ is Bragg's angle). The calculated average crystallite size is found to be 53 nm to 80 nm, which is shown in Table 1. It is noticed that crystallite size and intensity increase with increasing the concentration of Cu from X=0.00 to X=0.30. This depends on doping element percentage, temperature, growth atmosphere, crystallographic axes, and also quantum confinement effect.

Williamson-Hall (W-H) plots give crystalline size and lattice strain using this formula (33)-

$$B\cos\theta = \frac{k\lambda}{D} + 4\varepsilon \sin\theta \quad (2)$$

Since the Bragg diffraction peak width is a combination of instrumental integral width and the width broadening due to the materials. Therefore, the correct broadening of the diffraction peak of the sample is determined by using this formula bellowed (34)

$$\beta = [\beta^2_{measure} - \beta^2_{instrumental}]^{1/2}$$

Diffraction data of standard material (such as silicon, etc) was used to find out the instrumental integral width ($\beta_{instrumental}$), where β is full width at half maxima and ε is lattice microstrain and D is crystallite size. If we linear fit to the data of the graph plot between βCosθ and 4Sinθ (known as Williamson-Hall plots), the inverse of the intercept gives crystallite size and the slope gives lattice strain value. The lattice strain value of pure SnO_2 is found to be 1.058×10^{-3} and Cu doped SnO2 (0.10, 0.20, 0.30) is 1.352×10^{-3}, 1.415×10^{-3}, 1.527×10^{-3} respectively are given in table 2. It is observed that increasing the amount of Cu-doping decreases the lattice strain. We examined crystallite size calculated from Debye Scherer's formula is approximately the same value as the W-H plot.

The lattice parameter is calculated by this relation below-

$$\frac{1}{d^2} = \frac{(h^2+h^2)}{a^2} + \frac{(l^2)}{b^2}$$ - For Tetragonal structure (4)

Here a, b, and c are lattice parameters and it is given in Table 2 and see Fig 3 (a, b)

a=b=4.7348 c=3.1789 for X=0.00

a=b=4.7354 c=3.1822 for X=0.10

a=b=4.7365 c=3.1899 for X=0.20

a=b=4.7375 c=3.1920 for X=0.30

We observed lattice parameter is increased to increase the concentration of Cu due to the substitution of a larger Cu^{2+} ion (ionic radii is 0.73 Å) by a smaller Sn^{4+} ion (ionic radii is 0.69 Å) ion. So that lattice should be expanded. The formula of cell volume of the tetragonal structure is $a^2 \times c$, here a and c are lattice parameters, and here lattice parameter is already calculated in Table 2. Therefore we get the cell volume for pure SnO_2 is 71.2656($Å^3$), after doping of Cu concentration (0.10 to 0.30). It found 71.3576($Å^3$), 71.5625($Å^3$), 71.6409($Å^3$) respectively.

3.2 XPS (X-ray photoelectron spectroscopy)-

To analyze the chemical composition and chemical valence state of the sample ($Sn_{1-x}Cu_xO_{2-\delta}$) XPS has been carried out. The binding energies of Sn 3d, O 1s, C 1s, and Cu 2p core levels in pure and Cu-doped samples also have been identified by XPS. These binding energies are listed in Table 3. Fig 4(a) shows an XPS full-spectrum with high resolution of the pure and Cu-doped sample ($Sn_{1-x}Cu_xO_{2-\delta}$), which examined the C, O, Sn, and Cu peaks (with satellite peaks) present in my sample. Fig 4(b) shows XPS spectra with their binding energies of C 1s peaks obtained at 285.9eV due to the C–O bond after doping (Cu), its peaks are slightly at 288.6 (35). Fig 4(c) shows O 1s peaks are obtained at 531.3 eV of oxygen vacancy ($O\ 1_V$) of SnO_2 after Cu doping it shifts at 534. Some authors' result is very near to my result (36, 37). O 1s peaks are sifted because the polarizability of oxide ion is inverse purposely to O 1s binding energy in the XPS spectra of oxides when increased O 1s binding energy means decreased oxygen ion polarizability and a weak electron donor ability of the oxide ion (37). Fig 4(d) shows Cu $2p_{3/2}$ peaks are obtained at 933.3 eV and 953.3 eV for Cu $2p_{½}$ and two satellite peaks are observed at 942.8 eV and 962.5 eV of cu^{2+} state (38). Fig 8(e) shows Sn $^{4+}$ $3d_{5/2}$ and Sn $^{4+}$ $3d_{3/2}$ peaks are obtained at 487.2 eV and 495.5 eV respectively, which indicates that Sn atoms are present in the 4^+ valence state, after Cu doping it slightly shifts at 490.2 eV and 498.7 eV (38), Here all peaks are slightly sifted so we can verify that Cu doping is present in my sample.

4 - SURFACE MORPHOLOGY OF BULK

4.1- SEM (Scanning Electron Microscopy)

Fig 5(a-d) indicates SEM (Scanning Electron Micrographs) images of material have been calculated by IMAGE J software. ($Sn_{1-x}Cu_xO_2$) at x=0.00, 0.10, 0.20 particles are inhomogeneous, more aggressive, and densely closed with each other distributed over the surface (see Figs a, b, c). Finally, as the amount of Cu-dopant increases (x= 0.30) particles have mostly sheet-like shapes with few pores (see Fig d). The average particle size gradually increases from ~225 nm to 430 nm with increasing the Cu-doping in

SnO_2. The particle size observed by SEM is a larger value (due to agglomeration of the crystallites) from the XRD data. The small particle is converted into big clusters like the pomegranate shape because smaller particles have a broad surface free energy and would and larger particles to be formed. This is called the agglomeration process (39). Further, the shape of particles depends on the morphology, annealing temperature, atmosphere, etc of a sample.

4.2 TEM (Transmission electron microscopy) –

TEM is an experimental tool for the study of grain structure, grain size distribution, and crystalline nature of any sample. The transmission electron micrographs and the corresponding selected area electron diffraction (SAED) patterns for $Sn_{1-x}Cu_xO_2$ (x=0.00, 0.30) (powder) have been studied by IMAGE-J software in Fig 6 (a-d). The grain size is found approximately 20, and 90 nm for $Sn_{1-x}Cu_xO_2$ (x=0.00, 0.30) samples respectively and some cubic, spherical grains are present. We observed grain size is increasing due to Cu doping in the SnO_2 lattice. The SAED patterns (6a & 6c) show some sharp rings, which are indexed to the (110), (101), (211), and (301) planes of the SnO_2 rutile phase structure. Finally found that all the rings and spots matched with the SnO_2 rutile structure. It was examined by electron diffraction pattern.

5-OPTICAL PROPERTY-

5.1-UV-VIS Absorption Spectroscopy-

To understand the effect of Cu doping on optical properties of ($Sn_{1-x}Cu_xO_{2-\delta}$) nanomaterial by UV-Vis Spectroscopy (200-900nm) in absorption mode. We found the highest absorption at 304nm and decreased after 324nm (see, Fig 7 (a).

The optical band gap (E_g) is calculated with the help of the following formula (39)

$$\alpha = C\,\frac{(h\nu - Eg)^n}{h\nu} \qquad (5)$$

Where C is a constant that is different for different transitions indicated by different values of n. For direct transitions n = 1/2 or n = 2/3, for indirect transitions n = 2 or 3, depending on whether they are allowed or restricted. The band gap of the sample is obtained by extrapolation of the linear portion of the $(\alpha h\nu)^2$ vs $h\nu$ ($h\nu$ is photon energy) plot to $\alpha = 0$. The bandgap values (E_g) for the ($Sn_{1-x}Cu_xO_{2-\delta}$) samples at x = 0.00, 0.10, 0.20, 0.30 are found to be 3.531eV, 3.606eV, 3.660eV, 3.701eV respectively (as shown in fig 7 (b) and table 4). It is observed that the band gap of the samples increases with the increase in the concentration of copper (see Fig 7 c), it may be due to enhancement of oxygen vacancies. Since the oxygen vacancies increase due to the partial substitution of Sn^{4+} by Cu^{2+} ions or this is in agreement with the Burstein–Moss hypothesis (B- M hypothesis) (39, 40).

Urbach energy of the sample is calculated using the following equation-(41)

$$\alpha = \alpha_0 \exp\frac{E}{E_\mu} \qquad (6)$$

$$\text{Ln } \alpha = \text{Ln } \alpha_0 + \frac{E}{E_\mu} \quad (7)$$

Where α is the absorption coefficient, E is the photon energy, and E_μ is the Urbach energy. Urbach absorption is the absorption below the band gap. When defects in the system increase then absorption occurs below the band gap. Calculated Urbach energy is given in Table 4. We found that Urbach energy is found 0.1172 eV, 0.421eV 0.556eV, 0.687eV for ($Sn_{1-x}Cu_xO_{2-\delta}$) samples at x = 0.00, 0.10, 0.20, 0.30 respectively. Urbach energy increased which means that distortion also increased. The distortion occurs due to two reasons either copper is creating levels nearby conduction band or the incorporation of Copper in the system produces oxygen vacancies which are also creating levels nearby conduction band. (41). Fig 7 (d) shows a graph between optical bandgap v/s Urbach energy.

5.2-Raman Spectra of ($Sn_{1-x}Cu_xO_{2-\delta}$) nanoparticle-

The crystal structure and vibrational mode of ($Sn_{1-x}Cu_xO_{2-\delta}$) nanomaterial at x=0.00 and 0.30 are studied by Raman spectroscopy at room temperature (300 K) in the frequency range (200-1400 cm^{-1}). Which verifies that tetragonal crystal structure of my sample. In Table 5, According to group theory, there is total of 18 vibrational modes in SnO_2 for tetragonal structure. Since the normal modes are 3n (n=6 is the number of atoms in the primitive cell of SnO_2). In this way, only three Raman scattering modes, i.e., (A_{1g}, $B_{2g,}$ and doubly degenerate E_g) are available. Fig 8 shows, that the A_{1g} Raman active mode has a solid band at 631.75 cm^{-1} due to vibration of the Sn-O bond. After doping of Cu ions, the dominant bands of Sn-O are to be broad and have a slight shift from (631.75-634.61 cm^{-1}), and intensity also be increased because Cu-O starts to contribute with Sn-O since Cu-O also has a vibrational mode at 632 cm^{-1} in bulk nanoparticle and start to contribute with Sn-O bond (41) same result is shown by (35). B_{2g} Raman active mode has a small band at 774.34 cm^{-1} (41) after Cu doping it shifts at 776.60 cm^{-1} (42) due to the expanding and contracting scattering of the Sn-O bond. E_g active mode is very complex to oxygen vacancies compared with other modes and it has a vibration of two oxygen atoms it is active at 475.55 cm^{-1} after doping Cu ions it shifts at 476.60 cm^{-1} (42).

6- CONCLUSIONS

Pure and Cu-doped samples ($Sn_{1-x}Cu_xO_{2-\delta}$) have been synthesized by the solid-state reaction method and we inspected the structural, morphological, and optical characteristics. XRD examines the structure (rutile type tetragonal) of all compositions with neither impurities nor secondary phase. Crystallite size and lattice parameters were found to increase with Cu doping in SnO_2 lattice. SEM images confirm that SnO_2 particles are inhomogeneous, high aggregations, densely closed packed with each other and particle size is approximately 225-430nm. The TEM images show some cubic and spherical grains (~20, and 90 nm). UV-Vis spectroscopy examined that the band gap is found at 3.808eV and 3.912eV of ($Sn_{1-x}Cu_xO_{2-\delta}$) nanomaterial at X=0.10, x=0.30, which shows that band gap is also increased due to dopant ion and absorption peak is seen at 304nm as well as result of Urbach energy. The electronic state of Sn and Cu is 4^+ and 2^+ respectively analyzed by XPS. RAMAN investigates only three main vibrational modes, i.e., (A_{1g}, $B_{2g,}$ and doubly degenerate E_g) that are present in sample.

7. Acknowledgments:

I am very much grateful to Dr. Vasant G. Sathe, Centre-Director of UGC-DAE Consortium for Scientific Research (Indore, India.), Late Dr. Piyush Jaiswal (Physics department) and Prof. M. K. Dutta (Director Centre of Advanced Studies), Dr. A.P.J.A.K.T.U (Lucknow, India) for allowed to characterize the material.

References-

1. Marcos Fernández-Garcia, José A. Rodriguez, METAL OXIDE NANOPARTICLES, "Nanomaterials: Inorganic and Bioinorganic Perspectives" Brookhaven National Laboratory, 2007, BNL-79479-2007-BC.
2. George Fedorenko, Ludmila Oleksenko, and Nelly Maksymovych, Oxide Nanomaterials Based on SnO_2 for Semiconductor Hydrogen Sensor, Advances in Materials Science and Engineering, 2019, p 1-7, in English.
3. Venkataramana Bonu, Bhavana Gupta, Sharat Chandra, Arindam Das, Sandip Dhara, A. K. Tyagia, Electrochemical supercapacitor performance of SnO2 quantum dots, Electrochimica Acta, 2016, 203, p 230-237, in English.
4. Soumen Das, V. Jayaraman, SnO_2: A comprehensive review on structures and gas sensors, Progress in Materials Science, 2014, 66, p 112-255, in English.
5. Yu Huana, Xiaohui Wang, Tao Wei, Peiyao Zhao, Jing Xie, Zifan Yec, Longtu Li, Defect control for enhanced piezoelectric properties in SnO_2 and ZrO_2 co-modified KNN ceramics fired under reducing atmosphere, Journal of the European Ceramic Society, 2016, 37(5), p 2057-2065, in English.
6. Jun Song Chen and Xiong Wen (David) Lou, SnO_2-Based Nanomaterials: Synthesis and Application in Lithium-Ion Batteries, Small, 2013, 9(11), p 1877–1893, in English.
7. Yongzhao Wang, Xiaobo Hu, Ke Zheng, Xuhui Wei, Yongxiang Zhao, Effect of SnO_2 on the structure and catalytic performance of Co_3O_4 for N_2O decomposition, Catalysis Communications, 2018, 111, p 70–74, in English.
8. Detao Liu, Yafei Wang, Hao Xu, Hualin Zheng, Ting Zhang, Peng Zhang, Feng Wang, Jiang Wu, Zhiming Wang, Zhi Chen, and Shibin, SnO_2-Based Perovskite Solar Cells: Configuration Design and Performance Improvement, Solar RRL, 2019, 3(2), 1800292, in English.
9. Xingxuan Huang, Hongkang Wang, Chunming Niua and Andrey L. Rogach, SnO_2 nanoarrays for energy storage and conversion, Cryst Eng Comm, 2015, 17(30), p 5593–5604, in English.
10. Wang, Z., Nayak, P. K., Albar, A., Wei, N., Schwingenschlögl, U., & Alshareef, H. N., Transparent SnO–SnO_2 p–n junction diodes for electronic and sensing applications, *Advanced Materials Interfaces*, 2015, *2*(18), 1500374, in English.
11. Goutam Kumar Dalapati, abcde Himani Sharma, Asim Guchhait, Nilanjan Chakrabarty, Priyanka Bamola, Qian Liu, Gopalan Saianand, Ambati Mounika Sai Krishna, Sabyasachi Mukhopadhyay, Avishek Dey, Terence Kin Shun Wong, Siarhei Zhuk, Siddhartha Ghosh, Sabyasachi Chakrabortty, Chandreswar Mahata, Sajal Biring, Avishek Kumar, Camila Silva Ribeiro, Seeram Ramakrishna, Amit K. Chakraborty, Satheesh Krishnamurthy, Prashant Sonar and Mohit Sharma, Tin oxide for optoelectronic, photovoltaic and energy storage devices: a review. *Journal of Materials Chemistry A*, 2021, 9, p 16621-–16684, in English.
12. Murthy S. Chavali, Maria P. Nikolova, Metal oxide nanoparticles and their applications in nanotechnology, SN Applied Science, 2019, 1(16), p 1-30, in English.
13. Claudine nuguera, Metal oxide interfaces, Physics and Chemistry at outside surfaces, Cambridge core, 1996, p 128-159.
14. Amna Rafiq, Muhhamad Ali Tahir, Rabisa Zia, Kanwal nazir, Ayesha saheen, Sahid Mansoor, Waheed S. Khan, Imran Amin, Virus detection using nanobiosensors, nanosensor for nanoagriculture, metal oxide nanoparticles, 2022, p 547-572.
15. Sharadwata Pan, Thomas B. Goudoulas, Jaison Jeevanandam, Kei Xian Tan, Shamik Chowdhury, and Michael K. Danquah, Therapeutic Applications of Metal and Metal-Oxide Nanoparticles: DermatoCosmetic Perspectives. Front. Bioeng. Biotechnol, 2021, 9, p 724499, in English.

16. S. K. Tripathy, T. N. V. Prabhakar Rao, 2G The Influence of Annealing Temperature on Optical Properties of Tin Oxide (SnO_2), Thin Films Prepared by Thermal Evaporation Process, International Journal of Science and Research (IJSR), 2016, 5 (5), p 591-596, in English.

17. G.E. Patil, D.D. Kajale, S.D. Shinde, V.G. Wagh, V.B. Gaikwad, and G.H. Jain, Synthesis of Cu-doped SnO2 Thin Films by Spray Pyrolysis for Gas Sensor Application, Advancement in Sensing Technology, SSMI 1, 2013, p 299–311, in English.

18. M. Ali Yıldırım, Sümeyr, Tuna Yıldırım, Emine Fedakar, Aytunç Atesc, Synthesis, characterization and dielectric properties of SnO_2 thin films, Spectrochimica Acta Part A: Molecular and Biomolecular Spectroscopy, 2014, 133, p 60-65, in English.

19. V. Siva Jahnavi, Sumanta Kumar Tripathy, A.V.N. Ramalingeswara Rao, Structural, optical, magnetic and dielectric studies of SnO_2 nanoparticles in real-time applications, Physica B: Condensed Matter, 2019, 565, p 61–72, in English.

20. NITI YONGVANICH, AND SANTI MAENSIRI, Synthesis of Cobalt-Doped SnO2 Nanoparticles by Chemical Precipitation with Chelation, Integrated Ferroelectrics: An International, 2014, 156, p 53–57, in English.

21. Hyoun Woo Kim, Seung Hyun Shim, Chongmu Lee, SnO_2 microparticles by thermal evaporation and their properties, Ceramics International, 2006, 32, p 943–946, in English.

22. NUȚESCU DUDUMAN Catalina, BARRENA PÉREZ María Isabel, GÓMEZ DE SALAZAR Y CASO DE LOS COBOS José María, CARCEA Ioan, CHICET Daniela-Lucia and PALAMARCIUC Ion, Synthesis of SnO2 by Sol-Gel Method, Solid State Phenomena, 2016, 254, p 200-206, in English.

23. M. A. M. Akhir, S. A. Rezan, K. Mohamed, M. M. Arafat, A. S. M. A. Haseeb, H.L. Lee, Synthesis of SnO2 Nanoparticles via Hydrothermal Method and Their Gas Sensing Applications for Ethylene Detection, Materials Today: Proceedings, 2019, 17, p 810–819, in English.

24. Zeba Nasir, Mohammad Shakir, Rizwan Wahab, Mohd Shoeb, Parvez Alam, Rizwan Hasan, Khan Mohammad, Mobin Lutfullah Lutfullah, Co-precipitation synthesis and characterization of Co-doped SnO_2 NPs, HSA interaction via various spectroscopic techniques and their antimicrobial and photocatalytic activities, International Journal of Biological Macromolecules, 2017, 94, p 554-565, in English.

25. Agnks Smith, Jean-Marc Laurent, David S. Smith, Jean-Pierre Bonnet, Rafael Rodriguez Clemente, Relation between solution chemistry and morphology of SnO-based thin films deposited by a pyrosol process, Thin Solid Films, 1995, 266, p 20-30, in English.

26. H. Letifi, Y. Litaiem, D. Dridi, S. Ammar, and R. Chtourou, Enhanced Photocatalytic Activity of Vanadium-Doped SnO2 Nanoparticles in Rhodamine B Degradation, advances in Condensed Matter Physics, 2019, 2019, p 1-11, in English.

27. Sujata Roy, Homnath Luitel, D. Sanyal, Magnetic properties of transition metal doped SnO2: A detailed theoretical study, Computational Condensed Matter, 2019, e00393, in English.

28. Monika Duhan, Naveen Kumar, Anita Gupta, Anupinder Singh, Harminder Kaur, Enhanced room-temperature ferromagnetism in Cr and Fe co-doped SnO2 nanoparticles synthesized by sol-gel method, 2020,181, 109635, in English.

29. Yeonwoo Kim, SenaYang, Yeji Kang, Byung-Kwon Kim & Hangil Lee, Transition metal doped Sb@SnO2 nanoparticles for photochemical and electrochemical oxidation of cysteine, Scientific Reports, 2018, 8:12348, in English.

30. Suresh Sagadevan, Zaira Zaman Chowdhury, Mohd. Rafie Bin Johan, Fauziah Abdul Aziz, L. Selva Roselin, Jiban Podder, J. Anita Lett, and Rosilda Selvin, Cu-Doped SnO_2 Nanoparticles: Synthesis and Properties, Journal of Nanoscience and Nanotechnology, 2019, 19, p 7139–7148, in English.

31. Sara Benzitouni, Mourad Zaabat, Aicha Khial, Djamil Rechem, Ahlem Benaboud, Dhikra Bouras, Abdelhakim Mahdjoub, Mahdia Toubane, Raphael Coste, High Sensitivity of Porous Cu-Doped SnO2 Thin Films to Methanol, Advances in Nanoparticles, 2016, 5, 140-148, in English.

32. Danish Khan, Abdul Rehman, Muhammad Zahid Rafiq, Ahmed Muddassir Khan, Mohsin Ali, Improving the optical properties of SnO_2 nanoparticles through Ni doping by sol-gel technique, Current Research in Green and Sustainable Chemistry, 2022, 4, 100079, in English.

33. R.R. Awasthi, B. Das, Structural transition and tunable optical, morphological and magnetic properties of Mn-doped BiFeO3 films, Optik, 2019, 194, 162973, in English.

34. R. Awasthi, K. Asokan, B. Das, Effect of molar concentration on structural, magnetic domain and optical properties of $BiFeO_3$ thin films, Applied Physics A, 2019, 125(5), p 338-352, in English.

35. Hui Liu, An Wang, Quan Sun, Tingting Wang and Heping Zeng, Cu Nanoparticles/fluorine-doped Tin Oxide (FTO) Nanocomposites for Photocatalytic H2 Evolution under Visible Light Irradiation, Catalysts, 2017, 7, p 385-398, in English.

36. Shiqiang Zhou, Huapeng Wang, Jicu Hu, Tianping Lv, Qian Rong, Yumin Zhang, Baoye Zi Mingpeng Chen, Dongming Zhang, Jun Wei, Jin Zhang, and Qingju, Formaldehyde gas sensor with extremely high response employing cobalt-doped SnO_2 ultrafine nanoparticles, Nanoscale Adv., 2022, 4, p 824–836, in English.

37. Abdul Majid, James Tunney, Steve Argue, David Kingston, Michael Post, James Margeson Grae me, J. Gardner, Characterization of CuO phase in SnO_2–CuO prepared by the modified Pechini method, J Sol-Gel Sci Technol, 2010, 53, p 390–398, in English.

38. N Lavanya, S Radhakrishnan, N Sudhan, C Sekar, S G Leonardi, C Cannilla and G Neri, Fabrication of folic acid sensor based on the Cu doped SnO_2 nanoparticles modified glassy carbon electrode, nanotechnology, 2014, 25, p 1-9, in English.

39. Sushant Gupta, B.C. Yadav, Prabhat K. Dwivedi, B. Das, Microstructural, optical and electrical investigations of Sb-SnO2 thin films deposited by spray pyrolysis, Materials Research Bulletin, 2013, 48, p 3315–3322, in English.

40. Warda Darenfad, Noubeil Guermat, and Kamel Mirouh, Analysis of the effect of copper concentration on the structural, morphological, optical and electrical properties of Cu: SnO2 thin films, Prof. Dr. Umut ÖZKAYA, May 10-13, 2022(Konya, Turkey), ICEANS, 2022, p 775-795.

41. Pawan Chetri, Bhamyarswa Saikia, and Amarjyoti Choudhury, Structural and optical properties of Cu doped SnO2 nanoparticles: An experimental and density functional study Citation, J. Appl. Physics, 2013, 113(23), 233514, in English.

42. David Degler, Spectroscopic Insights in the Gas Detection Mechanism of Tin Dioxide Based Gas Sensors, 2017.

Tables

Table 1- Average Crystalline size (nm) from XRD data of ($Sn_{1-x}Cu_xO_{2-\delta}$) nanomaterials-

Nominal Concentration	Concentration of copper	Average Crystalline size (nm)
0.00	SnO_2	53
0.10	$Sn_{0.90}Cu_{0.10}O_{2-\delta}$	65
0.20	$Sn_{0.80}Cu_{0.20}O_{2-\delta}$	71
0.30	$Sn_{0.70}Cu_{0.30}O_{2-\delta}$	80

Table 2-The lattice parameters, cell volume, lattice strain of the pure and Cu-doped ($Sn_{1-x}Cu_xO_{2-\delta}$) nanomaterial-

Nominal Concentration	Concentration of copper	Sintering condition	Lattice parameter (Å) a=b	C(Å)	Cell volume ($Å^3$)	Lattice strain
0.00	SnO_2	900^0c for 7hr	4.7348	3.1789	71.2656	$1.058*10^{-3}$
0.10	$Sn_{0.90}Cu_{0.10}O_{2-\delta}$	1000^0c for 8hr	4.7354	3.1822	71.3576	$1.352*10^{-3}$
0.20	$Sn_{0.80}Cu_{0.20}O_{2-\delta}$	1000^0c or 8hr	4.7365	3.1899	71.5625	$1.415*10^{-3}$
0.30	$Sn_{0.70}Cu_{0.30}O_{2-\delta}$	1000^0c for 8hr	4.7375	3.1920	71.6409	$1.527*10^{-3}$

Table 3- The binding energies (eV) of Cu 2p, satellite peaks of Cu^{2+}, Sn 3d and O 1s, C 1s pure and Cu-doped ($Sn_{1-x}Cu_xO_{2-\delta}$) nanomaterial-

Concentration of copper	Satellite peak of Cu^{2+} (eV)	Satellite peak of Cu^{2+} (eV)	Cu $2p_{3/2}$ (eV)	Cu $2p_{1/2}$ (eV)	Sn $3d_{3/2}$ (eV)	Sn $3d_{5/2}$ (eV)	O 1s (eV)	C 1s (eV)
X=0.00					487.7	495.8	531.3	285.9
X=0.30	942.8	962.5	933.3	953.3	490.2	498.7	534	288.6

Table 4- Optical bandgap and Urbach energy of pure and Cu-doped ($Sn_{1-x}Cu_xO_{2-\delta}$) nanomaterial-

Concentration of cu	Band gap(ev)	Urbach energy (eV)
0.00	3.531	0.117
0.10	3.606	0.421
0.20	3.660	0.556
0.30	3.701	0.687

Table 5- Raman Active Mode in pure and Cu doped ($Sn_{1-x}Cu_xO_{2-\delta}$) nanomaterials-

Vibration mode	Pure SnO_2	Cu doped SnO_2 (x=0.30)
E_g	475.55	476.60
A_{1g}	631.75	634.61
B_{2g}	774.34	776.60

Figure captions

Figure 1 Flow chart of the formation ($Sn_{1-x}Cu_xO_{2-\delta}$) nanoparticle.

Figure 2(a) The powder x-ray diffraction pattern (XRD) of ($Sn_{1-x}Cu_xO_{2-\delta}$) nanoparticle at X=0.00, 0.10, 0.20, 0.30

Figure 3(a) lattice parameter (a=b) of ($Sn_{1-x}Cu_xO_{2-\delta}$) nanoparticle at X=0.00, 0.10, 0.20, 0.30

Figure 3(b) lattice parameter (c) of ($Sn_{1-x}Cu_xO_{2-\delta}$) nanoparticle at X=0.00, 0.10, 0.20, 0.30

Figure 4 (a) XPS survey spectra of ($Sn_{1-x}Cu_xO_{2-\delta}$) nanoparticle at X=0.00, 0.30

Figure 4 (b) XPS spectra of C 1s with their binding energies of ($Sn_{1-x}Cu_xO_{2-\delta}$) nanoparticle at X=0.00, 0.30

Figure 4 (c) XPS spectra of O 1s with their binding energies of ($Sn_{1-x}Cu_xO_{2-\delta}$) nanoparticle at X=0.00, 0.30

Figure 4 (d) XPS spectra of Cu 2p with their binding energies of ($Sn_{1-x}Cu_xO_{2-\delta}$) nanoparticle at X= 0.30

Figure 4 (e) XPS spectra of Sn 3d with their binding energies of ($Sn_{1-x}Cu_xO_{2-\delta}$) nanoparticle at X=0.00, 0.30

Figure 5 (a-d) Scanning electron microscopy images (SEM) of ($Sn_{1-x}Cu_xO_{2-\delta}$) at X=0.00, 0.10, 0.20, 0.30.

Figure 6 (a-d) Transmission electron microscopy images (TEM) and corresponding selected area electron diffraction (SAED) patterns of ($Sn_{1-x}Cu_xO_{2-\delta}$) at X=0.00 and 0.30.

Figure 7 (a) The absorption spectra of ($Sn_{1-x}Cu_xO_{2-\delta}$) at X=0.00, 0.10, 0.20, 0.30 nanoparticles.

Figure 7 (b) Plots of $(\alpha h\nu)^2$ versus ($h\nu$) of ($Sn_{1-x}Cu_xO_{2-\delta}$) at X=0.00, 0.10, 0.20, 0.30 nanoparticles.

Figure 7 (c) Plot of copper content versus optical bandgap (E_g) at X=0.00, 0.10, 0.20, 0.30 nanoparticle.

Figure 7 (d) Plot of optical bandgap (Eg) and Urbach energy versus copper content of ($Sn_{1-x}Cu_xO_{2-\delta}$) at X=0.00, 0.10, 0.20, 0.30 nanoparticle.

Figure 8 Raman Spectra of ($Sn_{1-x}Cu_xO_{2-\delta}$) at X=0.00, 0.30 pure and Cu-doped ($Sn_{1-x}Cu_xO_{2-\delta}$) nanomaterial.

Fig -1Flow chart of formation ($Sn_{1-x}Cu_xO_{2-\delta}$) sample at x=0.00, 0.10, 0.20, 0.30

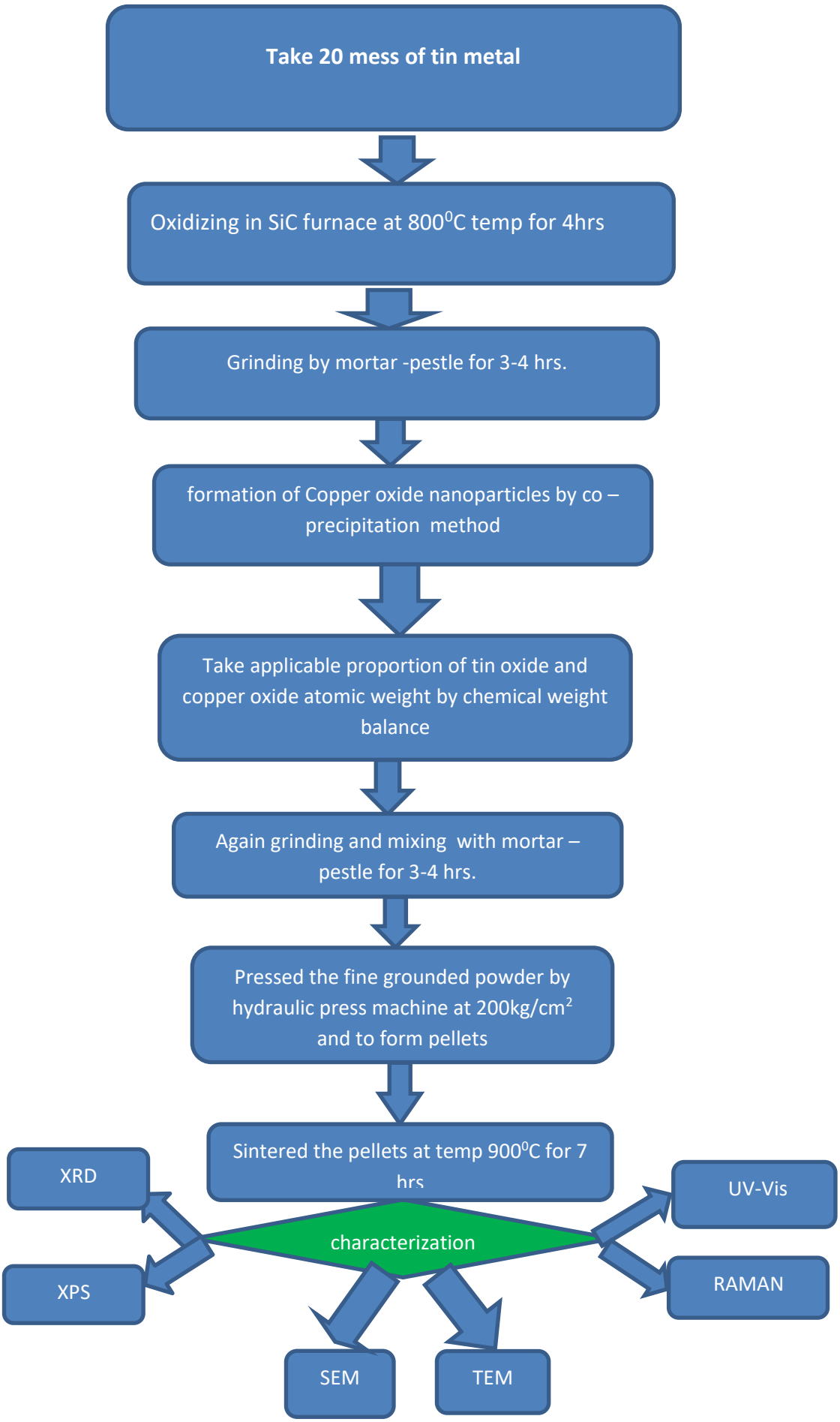

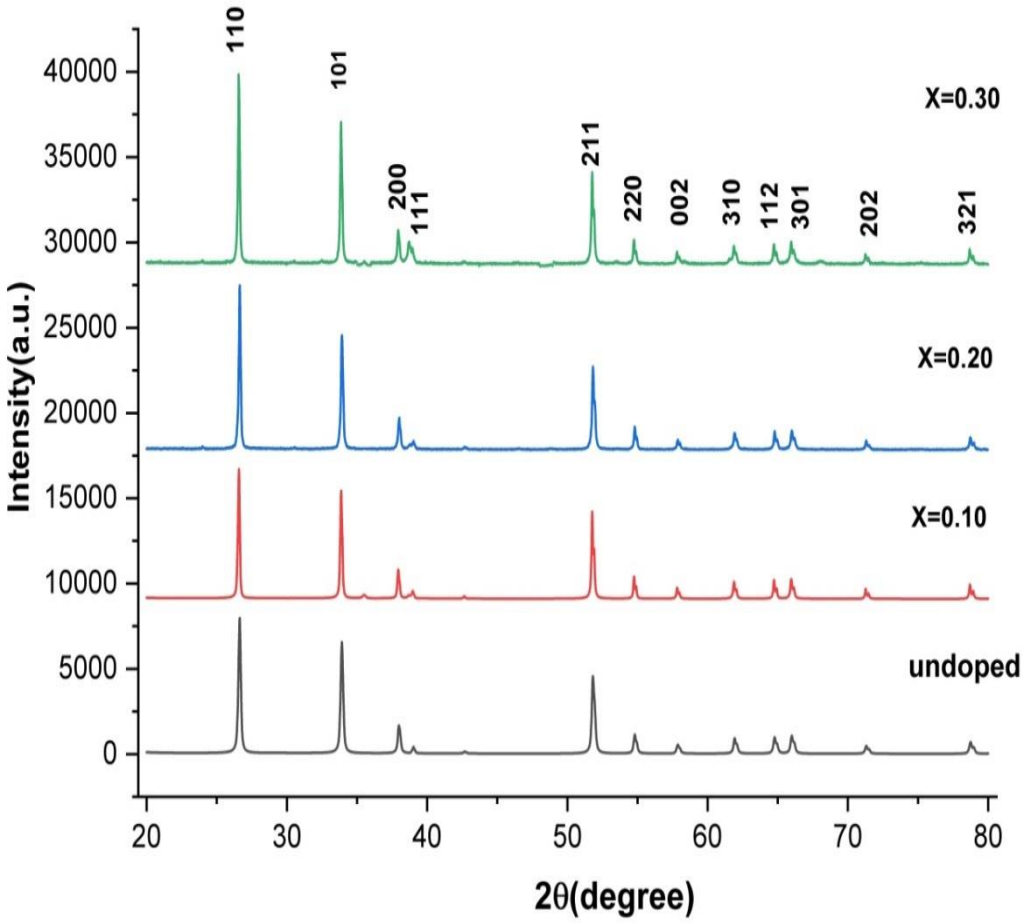

Fig-2 The powder x-ray diffraction pattern (XRD) of ($Sn_{1-x}Cu_xO_{2-\delta}$) nanoparticle at X=0.00, 0.10, 0.20, 0.30

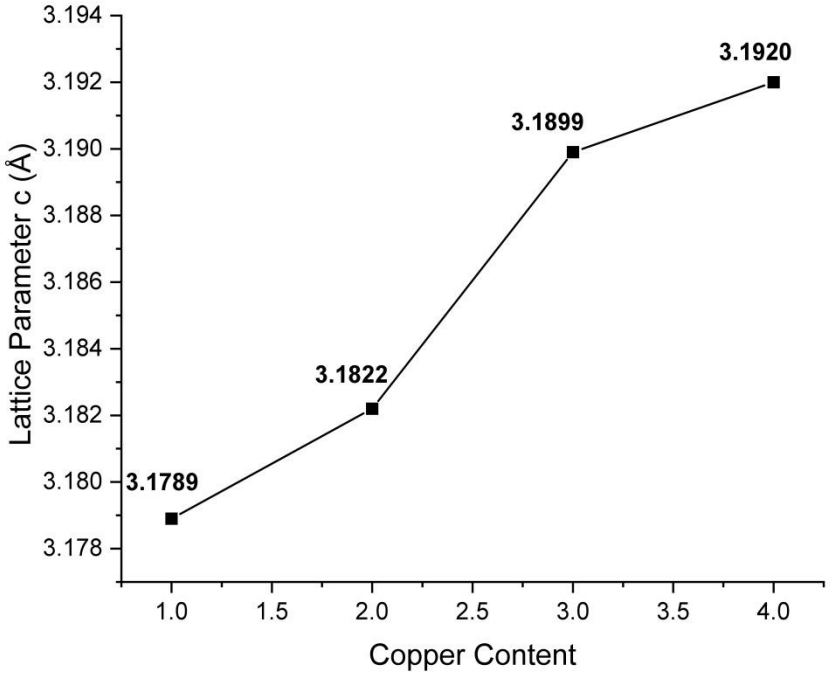

Fig- 3 (a) lattice parameter (a=b) of ($Sn_{1-x}Cu_xO_{2-\delta}$) nanoparticle at X=0.00, 0.10, 0.20, 0.30

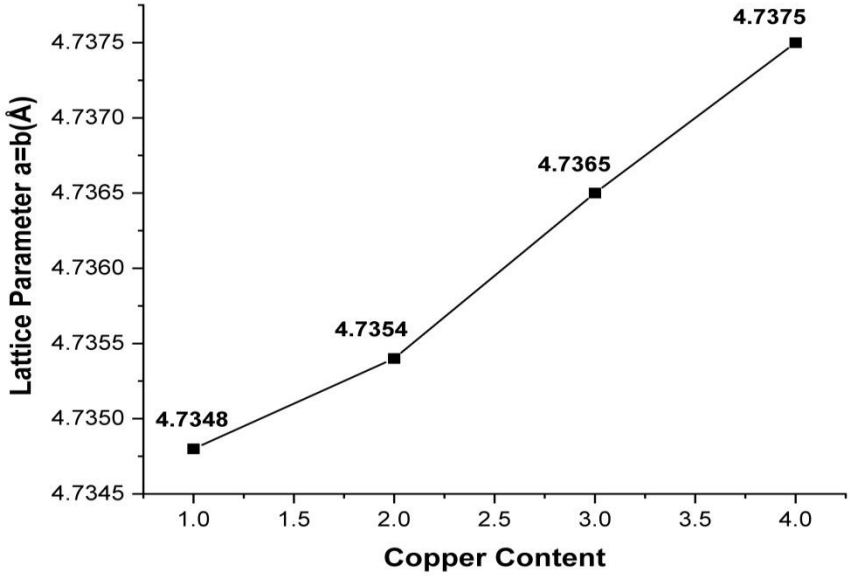

Fig-3 (b) lattice parameter (c) of ($Sn_{1-x}Cu_xO_{2-\delta}$) nanoparticle at X=0.00, 0.10, 0.20, 0.30

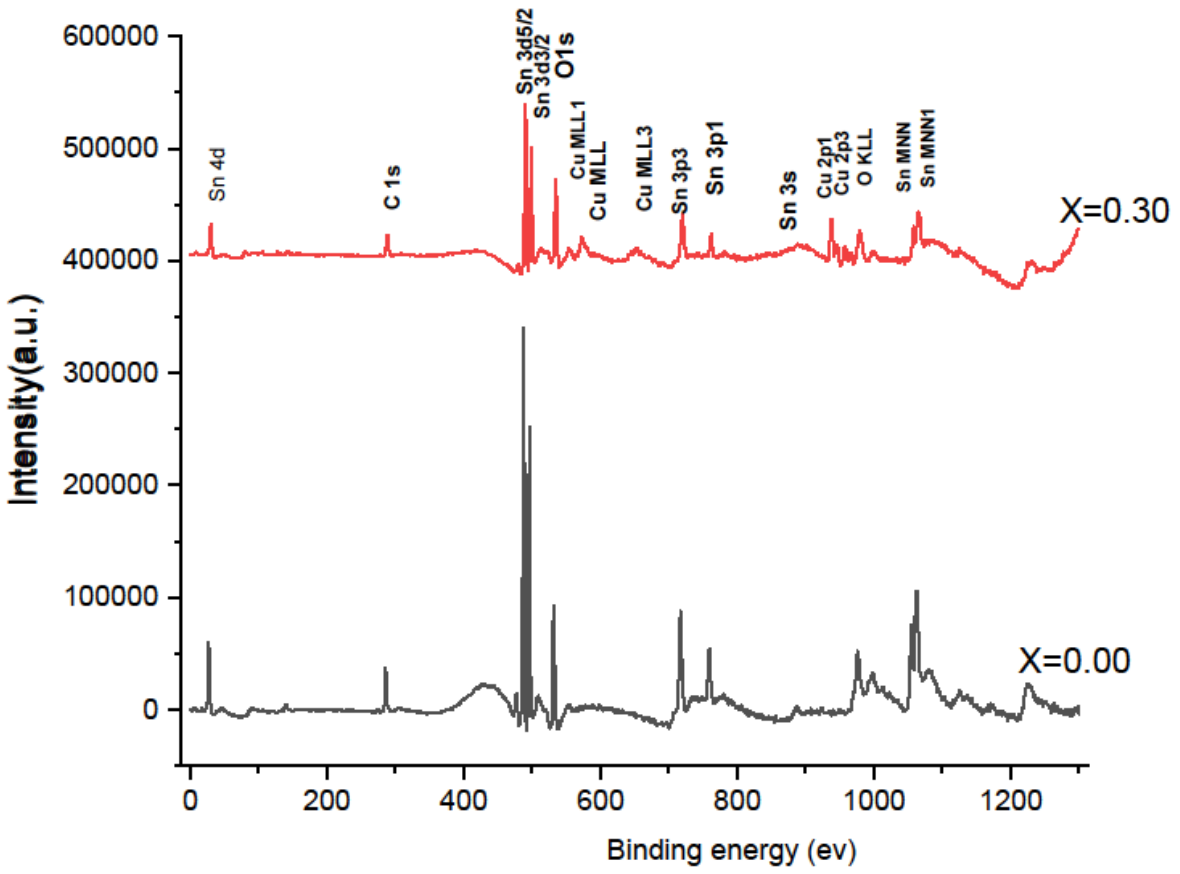

Fig-4(a) XPS survey spectra of ($Sn_{1-x}Cu_xO_{2-\delta}$) nanoparticle at X=0.00, 0.30

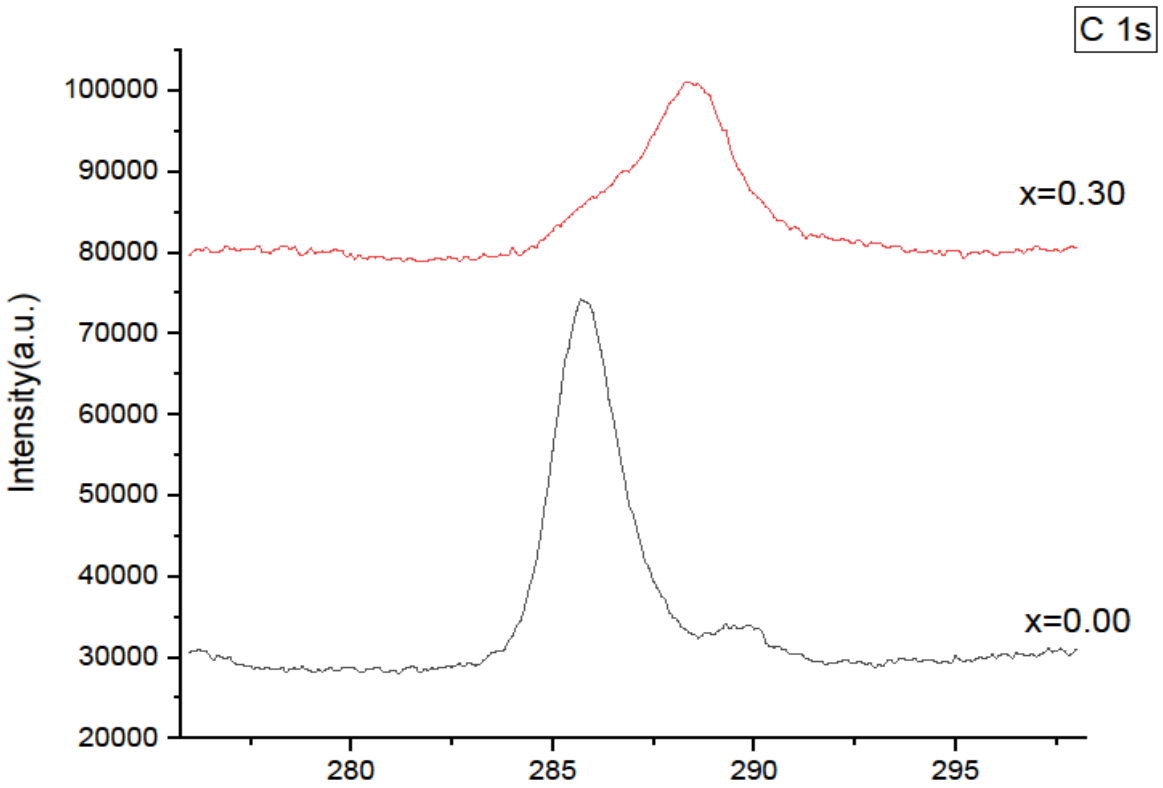

Fig 4 (b) XPS spectra of C 1s with their binding energies of ($Sn_{1-x}Cu_xO_{2-\delta}$) nanoparticle at X=0.00, 0.30

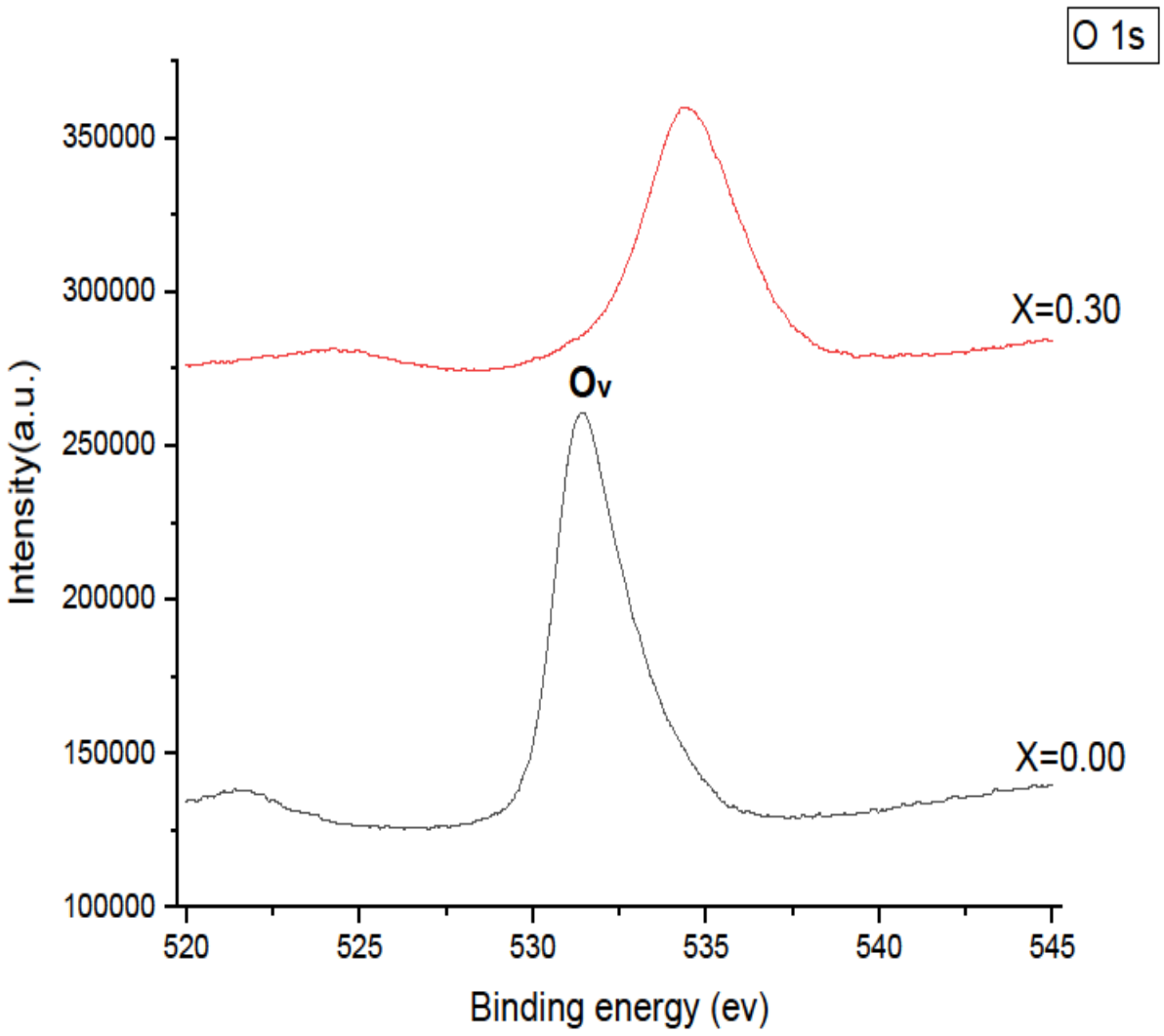

Fig 4 (C) XPS spectra of O 1s with their binding energies of ($Sn_{1-x}Cu_xO_{2-\delta}$) nanoparticle at X=0.00, 0.30

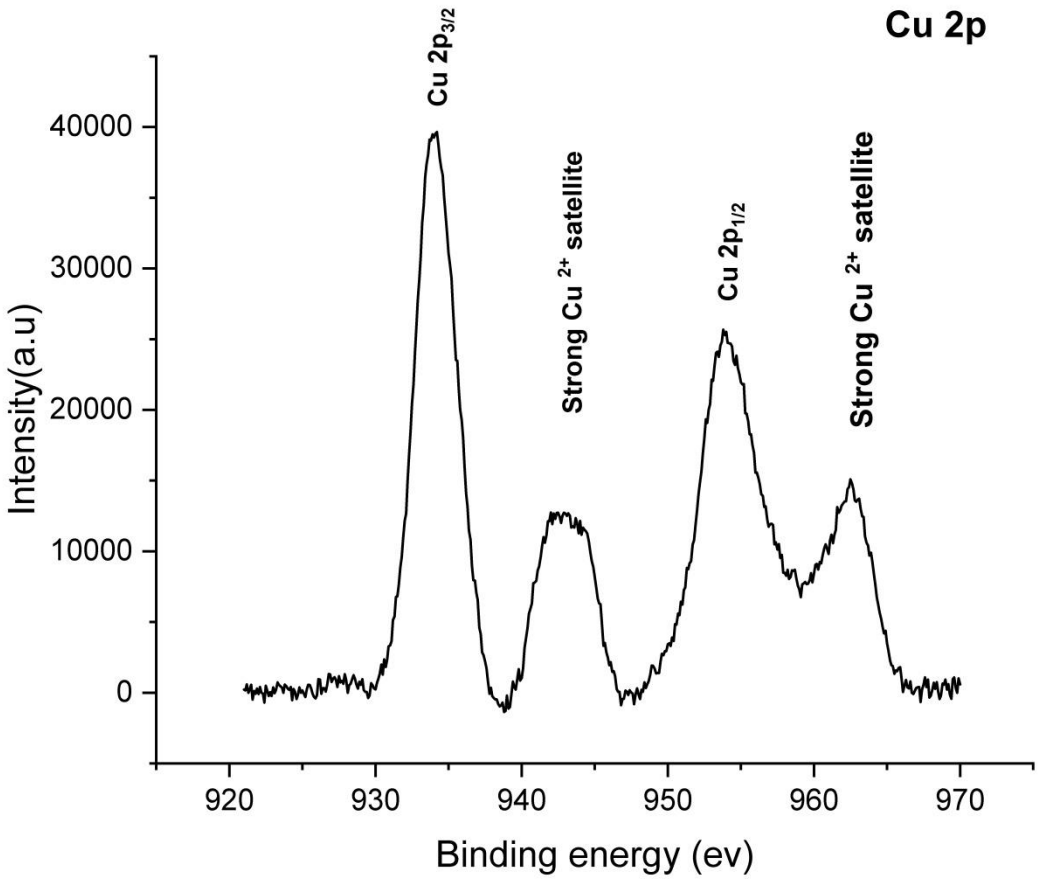

Fig 4 (d) XPS spectra of Cu 2p with their binding energies of ($Sn_{1-x}Cu_xO_{2-\delta}$) nanoparticle at X= 0.30

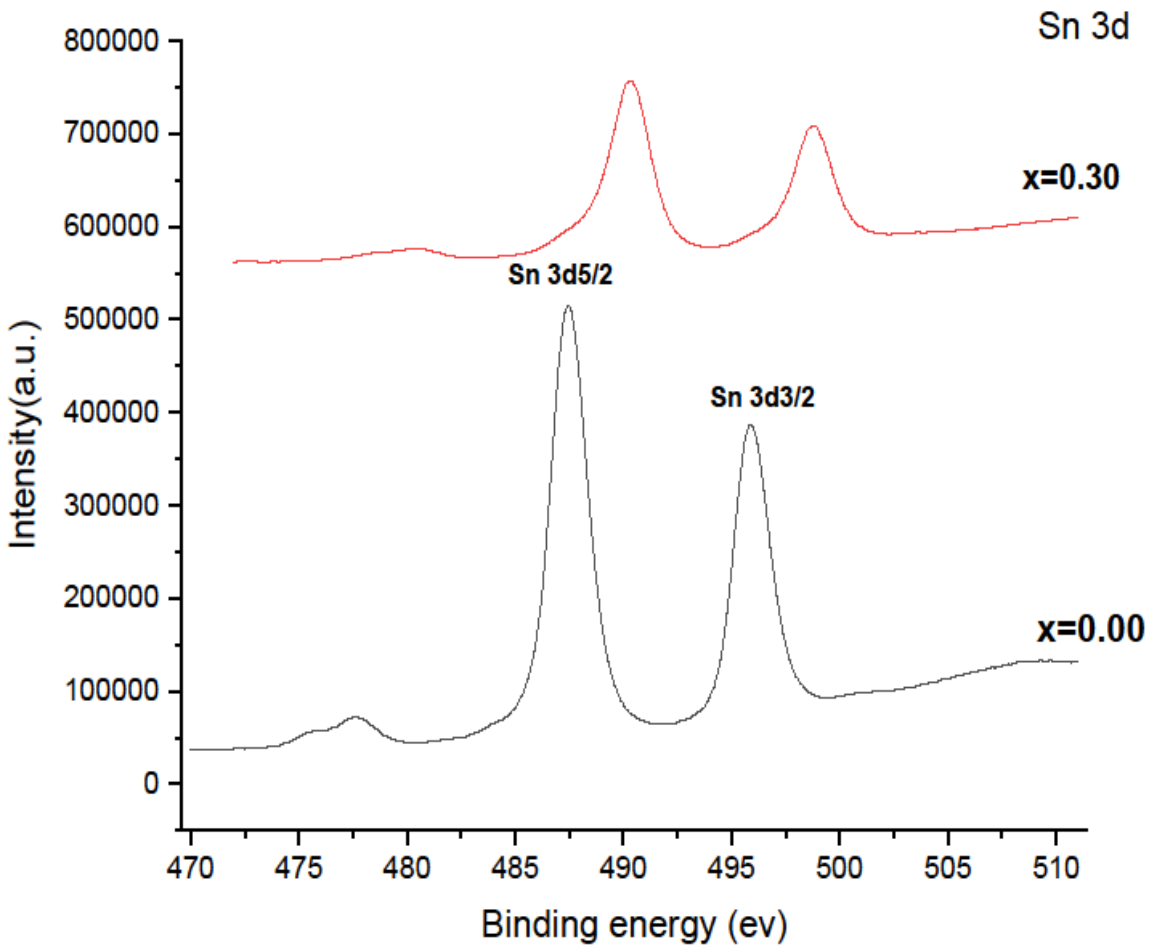

Fig 4(e) XPS spectra of Sn 3d with their binding energies of ($Sn_{1-x}Cu_xO_{2-\delta}$) nanoparticle at X=0.00, 0.30

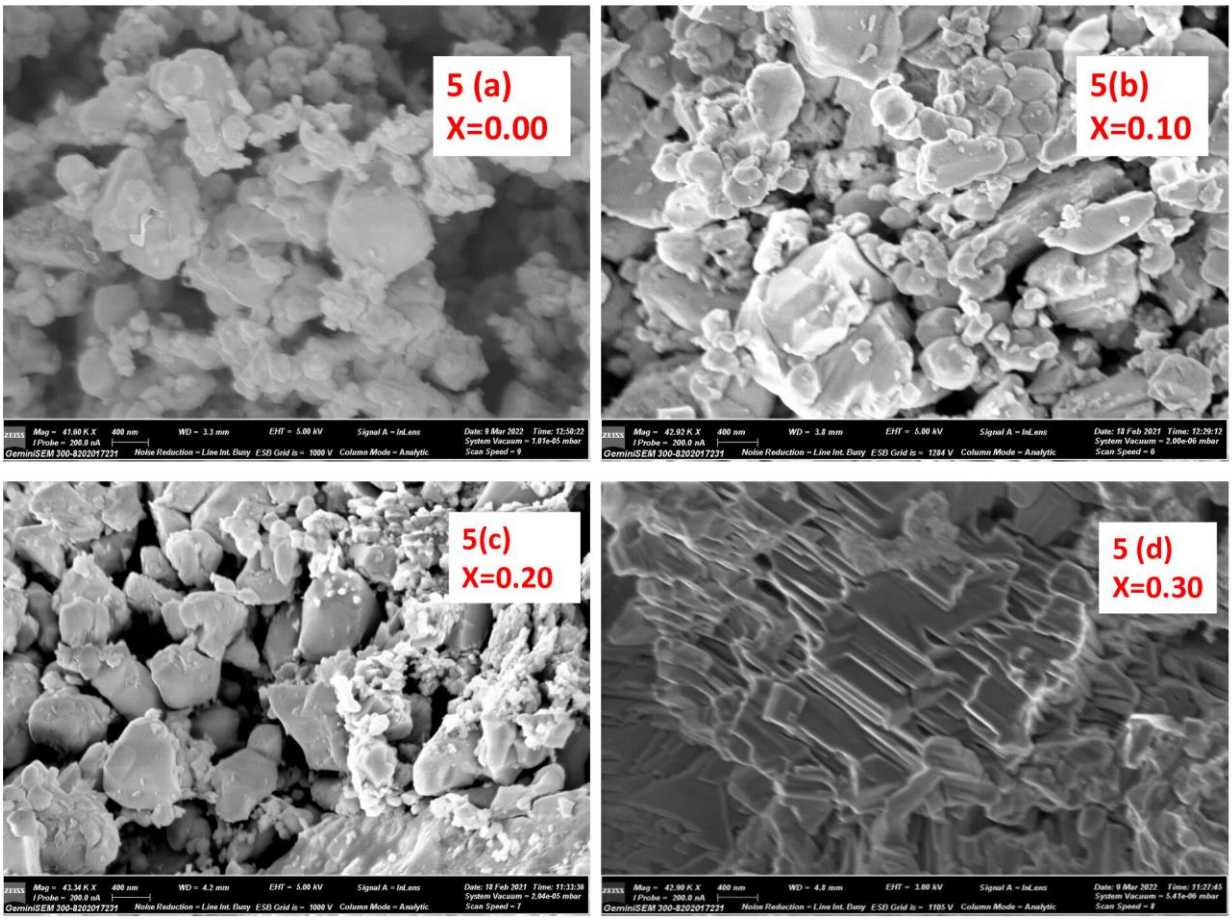

Fig 5 (a-d) Scanning electron microscopy images (SEM) of ($Sn_{1-x}Cu_xO_{2-\delta}$) at X=0.00, 0.10, 0.20, 0.30

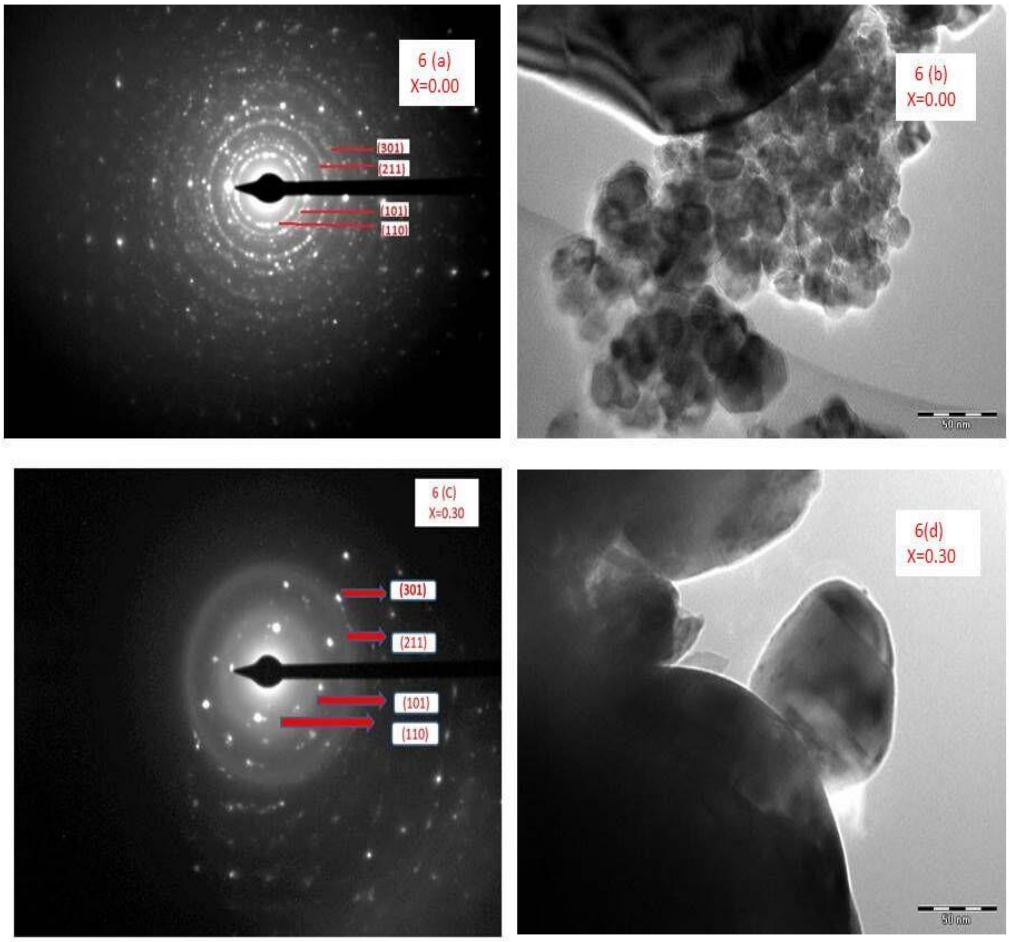

Fig 6 (a-d) Transmission electron microscopy images (TEM) and corresponding selected area electron diffraction (SAED) patterns of ($Sn_{1-x}Cu_xO_{2-\delta}$) at X=0.00 and 0.30

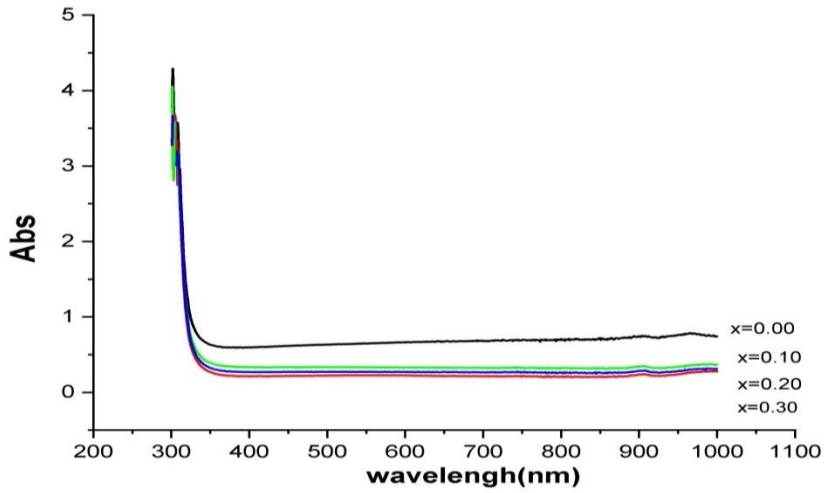

Fig 7 (a) Absorptionspectra of ($Sn_{1-x}Cu_xO_{2-\delta}$) at X=0.00, 0.10, 0.20, 0.30 nanoparticles

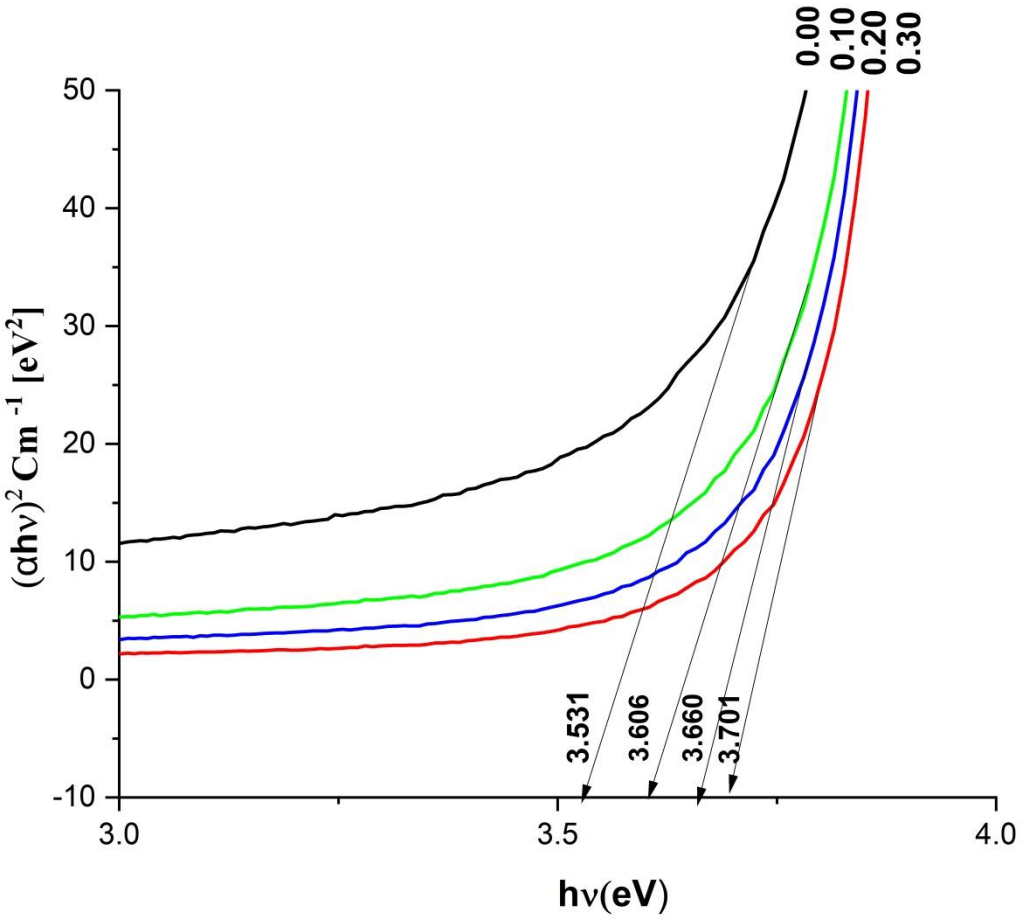

Fig 7 (b) Plots of $(\alpha h\nu)^2$ versus (hν) of $(Sn_{1-x}Cu_xO_{2-\delta})$ at X=0.00, 0.10, 0.20, 0.30 nanoparticles

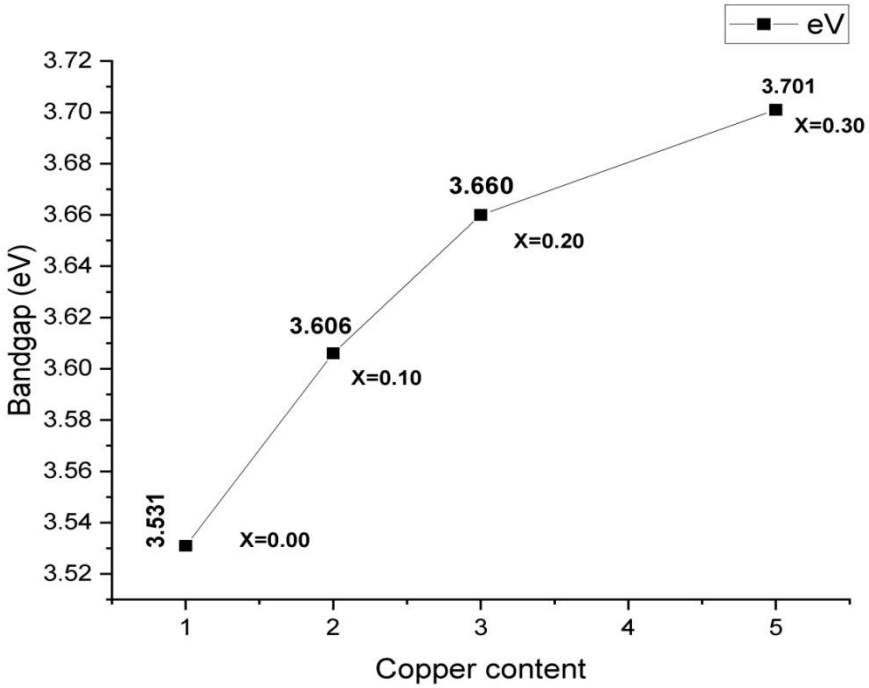

Fig 7 (c) Plot of copper content versus optical bandgap (E_g) at X=0.00, 0.10, 0.20, 0.30 nanoparticle

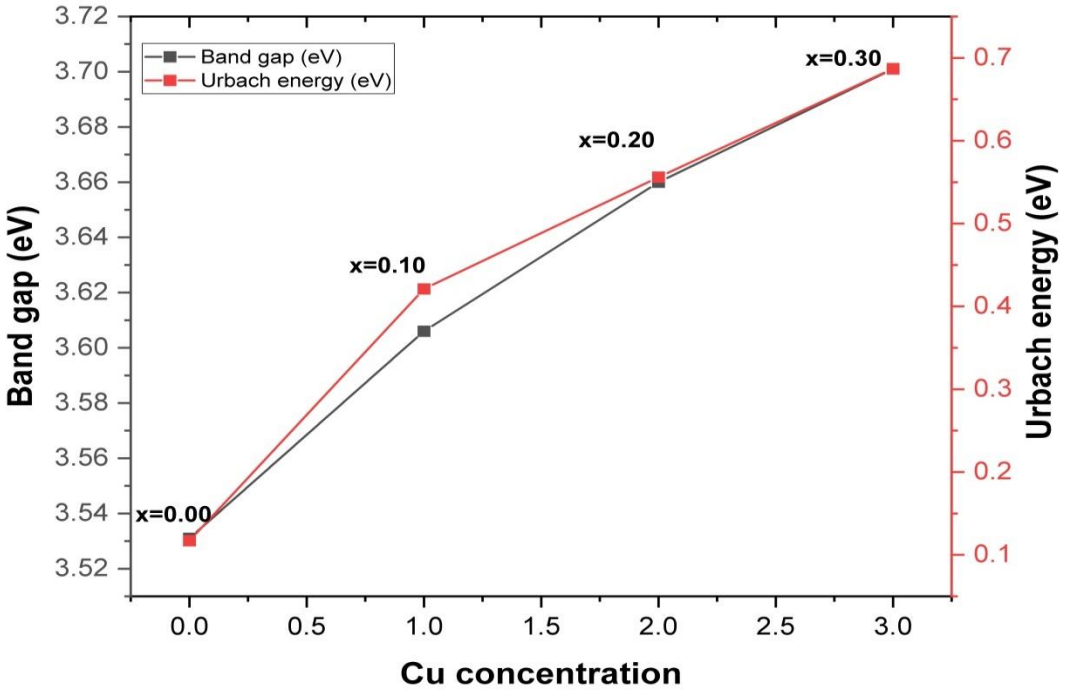

Fig 7 (d) Plot of optical bandgap (E_g) and Urbach energy versus copper content of ($Sn_{1-x}Cu_xO_{2-\delta}$) at X=0.00, 0.10, 0.20, 0.30 nanoparticle

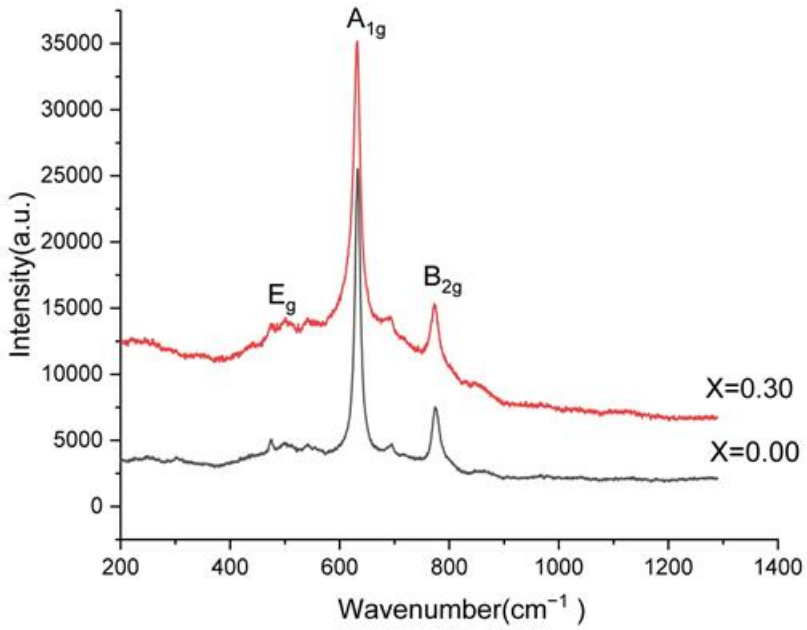

Fig 8 Raman Spectra of ($Sn_{1-x}Cu_xO_{2-\delta}$) at X=0.00, 0.30.